Solid particles focusing, orienting, and de-focusing in planar Poiseuille flow

J.J. Derksen

School of Engineering, University of Aberdeen, Aberdeen AB24 3UE, UK

jderksen@abdn.ac.uk

Submitted to AIChE J – March 2026; Revision submitted June 2026

Accepted July 2026

Abstract

Three-dimensional, time-dependent lattice-Boltzmann simulations of neutrally buoyant particles in planar Poiseuille flow have been performed. The particles are spherical or cylindrical (the latter with a length over diameter ratios in the range 1/3 to 2) and have volume fraction ranging from virtually zero (one particle) to 0.15. The channel's Reynolds number is in the range of 15 to 150. We first show agreement with earlier studies for single particle behavior in terms of lateral migration and orientation. We then show for the higher solids loadings to what extent particle-particle interactions influence focusing of particles and how – for cylinders – their orientations get distributed. The observed, and often strongly inhomogeneous, particle distributions as well as pronounced orientation distributions have an apparent impact on the flow resistance of the suspensions. We interpret the latter with help of the particle and liquid shear stress profiles over the height of the channel.

Topical heading

Transport Phenomena and Fluid Mechanics

Keywords

Particle migration; planar Poiseuille flow; particle-resolved simulation; non-spherical particles.

Data availability and reproducibility statement

The data presented here has been generated by in-house developed Fortran-based computer software; the supplementary material is an archive (.tar) file with the current version of this software with which data presented can be reproduced.

1. INTRODUCTION

There is extensive experimental and computational literature on the topic of laminar shear flows laden with solids migrating across streamlines thereby showing features such as preferential concentration ("focusing") and preferential orientation of the particles [1–6] with potential consequences for the suspension's rheological behavior [6]. Migration is driven by lift forces, which are inertial effects [7,8], i.e. they need a non-zero Reynolds number to occur. In earlier days, Segré and Silberberg [9] already reported on neutrally buoyant spheres laterally migrating to equilibrium radial positions in Poiseuille pipe flow along with an interesting discussion of the role of the Magnus force and a (then recently identified) lift force that now carries Saffman's name [8]. The advent of the research field of microfluidics has led to a renewed interest in lateral migration of particles in shear flow and is now being used for ordering and separation of particles in narrow channels [10–12].

Where many of the papers cited above focus on the behavior of an isolated particle in an inertial shear flow, we primarily have an interest in the behavior of a collective of particles and would like to find out to what level of solids loading single particle results remain accurate. The practical perspective of this is that particle focusing likely gets blurred or even changes fundamentally if particles strongly interact with one another and thus get hindered moving to their focus positions. This then would reduce the separation efficiency or (shape) selectivity if the system has been designed to act as such [12]. Another perspective for many-particle systems is a conjecture due to Saffman [7] that states that preferential orientation (of non-spherical particles) and preferential concentration will have consequences for the effective viscosity of suspensions.

Experimental work due to Han & Kim [13] reveals that for Poiseuille pipe flow with an overall solids volume fraction below 0.1 particles tend to migrate approximately to their single-particle equilibrium positions; at higher solids loadings particles behave very differently and concentrate near the centerline of the pipe. The latter effect was also observed in oscillatory pipe flow experiments by Snook et al [14]. In addition we note that the experimental images presented by Masaeli et al [15] show the behavior of closely spaced, and likely interacting, microscopic particles of various shapes in microfluidic ducts.

In this paper the sheared suspensions are approached computationally. In previous papers we have developed a simulation methodology for particle-resolved simulations of moderately dense to dense solid-liquid suspensions. This type of simulations has been pioneered by – among others – Feng et al [16] and Ladd [17,18]. Our simulations are three-dimensional, time-dependent lattice-Boltzmann (LB) simulations with solid particle sizes larger, by at least one order of magnitude, than the lattice spacing (i.e. the space resolution of the liquid flow). The no-slip conditions at the surfaces of the particles are imposed by an immersed boundary (IB) method. Starting point is a planar Poiseuille flow (laminar flow between two flat parallel plates driven by a pressure gradient) that we subsequently load with spherical or cylindrical particles.

After demonstrating confidence in the simulation method by reproducing qualitatively and quantitatively single particle migration results from the literature [19,20] we move to studying multi-particle systems. The paper then aims at quantifying location and – for non-spherical particle – orientation dispersion as impacted by particle-particle interactions as a function of the overall solids volume fraction and as a function of the Reynolds number (the latter based on the maximum particle-free flow velocity and channel width). It is finally shown how the presence of particles – including their spatial and orientational distribution – affects the resistance to flow / effective viscosity of the suspension.

2. FLOW SYSTEM

The flow domain has length L in the streamwise (x) direction, width W in the spanwise (y) direction, and height H in the wall-normal (z) direction; with $L=2H$ and $W=H$. Top and bottom of the domain (at $z=0$ and $z=H$) are rigid, no-slip walls. Periodic conditions apply in the x and y direction. The flow of the Newtonian liquid with density ρ and kinematic viscosity ν is due to a body force f_x in the x-direction. This generates a Poiseuille flow with x-velocity $u_x = f_x z\left(H-z\right)/\left(2\rho\nu\right)$; the centerline velocity thus is $U = f_x H^2 / (8\rho\nu)$. This channel's Reynolds number is defined as $\mathrm{Re} = UH/\nu$. It has been set to four values: $\mathrm{Re} = 150, 60, 30, \text{and } 15$.

In this domain we release a number of solid particles; either spheres with diameter d, or cylinders with diameter d_c and length ℓ that we have chosen such that their equivalent diameter $d_e = \sqrt[3]{3d_c^2\ell/2}$ is equal to the diameter of the spheres, i.e. $d_e = d$, so that spheres and cylinders take up the same volume. The particles have an appreciable size as compared to the channel height: $d_e = d = 0.133H$. The aspect ratios of the cylinders range from $\ell/d_c = \frac{1}{3}$ to $\ell/d_c = 2$. The particles have a density ρ_p such that $\gamma \equiv \rho_p/\rho = 2.0$. Gravity (in *z*-direction) has not been considered in order to limit the dimensionality of the parameter space. Without gravity the density of the particles is a parameter with minor impact on overall system behavior. It is acknowledged that if we were to involve experimental validation with horizontal channels, gravity would need to be included in the simulations.

We have run single-particle simulations as well as multi-particle simulations. In the latter the particles are placed randomly – in a non-overlapping fashion – in the flow domain with an overall solids volume fraction $\langle\phi\rangle$ that ranges from 0.00625 to 0.15.

3. SIMULATION APPROACH

The simulations make use of a variant of the lattice-Boltzmann (LB) method [21] due to Somers and Eggels [22,23]. It numerically solves the time-dependent Navier-Stokes equations in three dimensions on a uniform, cubic grid of nodes with spacing Δx. The algorithm steps in time with a step Δt. The spatial resolution is such that $H = 120\Delta x$ (which implies $d = d_e = 16\Delta x$); the time step is such that $U\Delta t/\Delta x = 0.075$. This low value of the Courant number is required to make sure that the Mach number is sufficiently small to approximate incompressible flow with the compressible numerical method LB is.

The solid particles in the flow domain are represented by densely spaced (typical nearest neighbor spacing of $0.6\Delta x$) marker points on their surface. The immersed boundary (IB) method [24,25] uses these points to locally calculate forces on the fluid that make the fluid have the same velocity as the solid surface, thus imposing the no-slip condition at the particle surface. Integrating the force distribution over a particle surface results in the overall hydrodynamic force and torque the particle exerts on the fluid. The opposite force and torque are what the fluid exerts on the particle, and this then feeds in the equations of translational and rotational motion we solve for each particle.

In addition to hydrodynamic force and torque, the particles feel forces and torques due to short-range particle-particle and particle-wall interactions: contact and lubrication. The lubrication force is needed to compensate for the finite resolution of the computational grid. If two solid surfaces move closer than $\mathrm{Order}(\Delta x)$, the flow in between the surfaces is not properly resolved by the LB method anymore and therefore the strength of the hydrodynamic interaction gets underestimated [26]. Explicitly including analytical low-Reynolds number expressions for lubrication interactions [27] mitigates this issue [28]. Contact forces prevent particle volumes overlapping and achieve "dry" friction with a friction coefficient μ_f that was set to 0.25. When particle surfaces get closer than a certain distance, typically $5 \cdot 10^{-3} d_e$, elastic springs get activated that push the surfaces apart and – in case of non-zero friction coefficients between solid surfaces – apply tangential forces. The marker points, as already used for the IB method, are used for detecting closeness of solid surfaces. Close-range interactions are triggered when marker points on two different particle surfaces get within a certain distance. Detailed expressions for the short-range forces as well as the settings of the parameters involved, such as spring constants and close-distance threshold values, are to be found in previous works [29,30] as well as in Supporting material Table S1.

Newton's and Euler's equations of translational and rotational motion respectively are used to update linear and angular particle velocities with a split-derivative [31] time-discretization method that can achieve the same time step Δt as the LB updates. Particles are then displaced according to an Euler-forward scheme. The particle orientations make use of quaternions [32] that are updated by integration using the angular velocities over time step Δt.

4. RESULTS

4.1 Single particle migration

We start our discussion of the results with a single sphere in the Poiseuille channel. It is released at two different initial z-locations: $z_0/H = 0.1$ and 0.4. Time series $z(t)$ for a number of scenarios can be seen in Figure 1. At time zero, the liquid was given the undisturbed parabolic Poiseuille velocity profile and the sphere was given the linear velocity of the undisturbed liquid at its center location and zero rotational velocity. The time series then indicate that, irrespective of the release location, the sphere migrates to a stable location that depends on the Reynolds number: z_∞/H =0.215, 0.224, 0.235, and 0.274 for $\mathrm{Re} = 150$, 60, 30, and 15 respectively. It is informative to consider the timescales over which the migration occurs: the lower the Reynolds number, the longer it takes, in dimensionless time tU/d, for the sphere to reach its ultimate z-location. The high end of the time axis of Figure 1 (tU/d=4.5·10^3) corresponds to $\sim 10^6 \Delta t$. The stable sphere locations agree well with those reported by [18] for comparable values of the Reynolds number and given the sphere diameter to channel height ratio d/H. For instance, interpolating their data in their Figure 4 at $a/H = \frac{1}{2} d/H = 0.0667$ gives z_∞/H =0.242; compare this to z_∞/H =0.235 at Re=30 we found.

Non-spherical particles not only migrate, they also evolve in terms of their orientation. This is demonstrated by a cylinder with $\ell/d_c = 1$ at $\mathrm{Re} = 150$ in Figure 2. It starts at $z_0/H = 0.1$, as before, in a developed Poiseuille flow. We now vary its initial orientation. Initial orientation is defined by the unit vector $\mathbf{a}_0$ which is the vector along the centerline of the cylinder at time zero. If the cylinder is released with its centerline coinciding with the direction of shear, i.e. the y-direction $\mathbf{a}_0 = \begin{pmatrix} 0 & 1 & 0 \end{pmatrix}$, Figure 2 shows that the cylinder maintains this orientation and, while *spinning* around its centerline, migrates to z_∞/H =0.215. We should here mention that this simulation has been continued well beyond the high-end of the time axis of Figure 2 (actually until tU/d =4.2·10^3) without observing the cylinder changing its orientation. The same cylinder released with the centerline along the x-axis rotates around the y-axis and thereby *tumbles* to a slightly larger stable (apart from a very slight oscillation) z-position z_∞/H =0.226.

In an intermediate case with $\mathbf{a}_0 = \left(-\frac{1}{3} \quad \frac{2}{3} \quad \frac{2}{3}\right)$, the cylinder fairly quickly orients to a tumbling mode; see the lower panel of Figure 2 that shows two of the cylinder's centerline vector components $\mathbf{a} = \left(a_x \quad a_y \quad a_z\right)$ as a function of time. Component a_y quickly goes to zero and a_x takes on a sinus function. The above thus shows a sensitivity of the fate of an $\ell/d_c = 1$ cylinder for its initial orientation.

The evolution of the orientation of cylinders with $\ell/d_c \neq 1$ is shown in Figure 3. The top panel shows that a cylinder with $\ell/d_c = \frac{1}{2}$ (a disk) with its centerline initially oriented along the *x*-axis evolves into a spinning motion with the centerline oriented along the shear direction (*y*) where that transition takes more time for the lower Reynolds number (Re=30). The same preferential orientation was observed by Nizkaya et al [20] who simulated oblate spheroids in planer Poiseuille flow.

The bottom panel of Figure 3 shows two short rods ($\ell/d_c = \frac{3}{2}$ and $\ell/d_c = 2$) that start oriented along the *y*-axis. They change their orientation so that a_y becomes zero and then tumble, rotating around the *y*-axis, where the shorter of these two cylinders takes more time to make this transition.

Table 1 summarizes the fate of the various single cylinders we have been investigating. There are minor differences in their stable *z*-location. All cylinders eventually reach a spinning ($|a_{y\infty}|$=1) or a tumbling ($|a_{y\infty}|$=0) state. Disks with $\ell/d_c \leq \frac{2}{3}$ spin; rods with $\ell/d_c \geq \frac{3}{2}$ tumble. In intermediate cases their eventual state depends on their initial orientation. The cylinder with $\ell/d_c = 0.86$ is a special case in the sense that it has identical moments of inertia over its three principal axes.

Table 1. Eventual *z*-location and orientation of cylinders as a function of ℓ/d_c and Re.

ℓ/d_c	Re	z_∞/H	$\lvert a_{y\infty}\rvert$
1/3	150	0.240	1
1/2	150	0.228	1
1/2	30	0.232	1
2/3	150	0.223	1
0.86*	150	0.223^t 0.217^s	0 or 1**
1	150	0.226^t 0.216^s	0 or 1**
3/2	150	0.233	0
2	150	0.242	0

* $I_1 = I_2 = I_3$ **depends on initial orientation t: tumbling s: spinning

4.2 Multi-particle systems

In the same Poiseuille channel, n spheres – all having the same diameter d – were randomly released such that their volumes were not overlapping. The overall solids volume fraction $\langle\phi\rangle = \frac{\pi n d^3}{6HLW}$ was varied from 0.00625 (10 spheres) to 0.15 (240 spheres). The initial condition is the same as for the one-sphere simulations: a parabolic velocity profile for the liquid and the spheres having the *x*-velocity of the undisturbed liquid at their center location and zero angular velocity. We let that system evolve in time while we monitor the solids volume fraction distribution in the *z*-direction $\phi(z)$. This is done with the spatial resolution of the LB grid; for every cubic grid cell (with size $\Delta x = d/16$) we check if its center is covered by a sphere and then average over the homogeneous *x* and *y* directions and over time (typically over a time period of $t \approx 500\, d/U$) to obtain $\phi(z)$. We report the solids concentration profile once it is stable, which for $\mathrm{Re} = 150$, takes of the order $t = 10^3\, d/U$. This time is comparable to the timescales observed for migration of a single sphere at this Reynolds number. The time we allow the system to reach steady state and the averaging times per Reynolds number have been specified in Table S2. Sample results for $\mathrm{Re} = 150$ are shown in Figure 4.

For the lower two $\langle\phi\rangle$ values the spheres migrate close to their stable single-sphere *z*-positions. The $\phi(z)$ peak locations for $\langle\phi\rangle$=0.0125 are $z/H = 0.213$ and 0.788 (i.e. 0.212 from the top wall); for $\langle\phi\rangle$=0.025 they are $z/H = 0.204$ and 0.796 (0.204 from top wall). Compare this to $z_\infty/H = 0.215$ for a single sphere at $\mathrm{Re} = 150$ (see Figure 1). At $\langle\phi\rangle$=0.10 the solids concentration peaks have widened; however, there still are *z*-regions where the solids preferentially concentrate while they avoid the middle of the channel. This then changes significantly when we go to $\langle\phi\rangle$=0.15 that – contrary to the cases with less overall solids loading – shows a concentration profile with actually a minor preference for solids in the middle of the channel (*core-peaking*).

The velocity contours in Figure 4 indicate that the presence of the particles slows down the flow significantly, i.e. increases the flow resistance. To indicate the level of flow reduction, the caption of Figure 4 includes values of the Reynolds number based on the superficial velocity $\mathrm{Re}_{sup} = u_{sup} H / \nu$.

It appears that core-peaking, next to depending on the solids loading, is a pronounced function of the Reynolds number. Figure 5 contains a matrix of concentrations profiles as a function of Re, increasing from left to right, and of $\langle \phi \rangle$, increasing from top to bottom. At $\langle \phi \rangle$=0.0125 the spheres clearly focus towards their stable positions, almost irrespective of the Reynolds number. At higher $\langle \phi \rangle$ first the preferential concentration peaks get wider, after which the center of the channel, that was (almost) void of solids at low $\langle \phi \rangle$, now becomes a preferred location for particles. This transition with increasing $\langle \phi \rangle$ happens sooner for lower Reynolds number. This has been observed experimentally by [13] for axisymmetric Poiseuille flow, where they used magnetic resonance imaging (MRI) imaging, for solids volume fractions in the range $\langle \phi \rangle = 0.06$ to 0.4. They measured a transition from off-core to core solids concentration peaking going from $\langle \phi \rangle = 0.06$ to 0.1; initially for their lowest Reynolds numbers (note that their Reynolds numbers are – different from ours – based on particle radius and average duct velocity) and then at still higher $\langle \phi \rangle$ also for higher Reynolds numbers. This is in agreement with our results where it needs to be kept in mind that they had axisymmetric Poiseuille flow and we have planar Poiseuille flow.

We now turn to the collective behavior of rigid solid particles of cylindrical shape. In the first instance we focus on three types of cylinders: $\ell / d_c = \frac{1}{2}, 1,$ and 2; each type of cylinder has the same volume. In addition to preferential concentration, cylinders show preferential orientation. To characterize the latter, we define the angle ψ_y as the angle between the *y*-axis (the shear direction) and the cylinder's centerline. A collection of cylinders with random isotropic orientation have a distribution of ψ_y according to $\sin \psi_y$, with ψ_y in the range $0 - \pi/2$.

Qualitatively cylinders with ℓ/d_c =1 behave in terms of preferential concentration as the spheres did. In Figure 6 it is shown that at low $\langle\phi\rangle$ they concentrate at their single-particle stable locations and make a similar transition to more even concentration distribution and core peaking (at least for $\mathrm{Re}=30$) at higher $\langle\phi\rangle$. In Figure 2 it was shown that a single cylinder with ℓ/d_c =1 in Poiseuille flow had at least two stable orientations (in line with, or perpendicular to the shear direction, i.e. ψ_y=0 or $\pi/2$). It shows that a multitude of such cylinders suspended in Poiseuille flow at low $\langle\phi\rangle$ strongly favor their centerline to be perpendicular to the shear direction. Increasing $\langle\phi\rangle$ leads to wider angle distributions and less pronounced preferential orientations at both $\mathrm{Re}=150$ and 30.

If we compare the behavior of disks (ℓ/d_c =0.5) and rods (ℓ/d_c =2) at $\mathrm{Re}=150$, as we do in Figure 7, we see the same trends when it comes to $\phi(z)$, and at the same time significant differences in orientation. Disks align their centerline with the shear direction, rods have their centerline perpendicular to the shear direction. The strength of this preference quickly weakens with increasing $\langle\phi\rangle$.

4.3 Flow resistance and effective viscosity

For a given body force, the volumetric flow rates of the particle laden cases are consistently lower than the single-phase flow rate implying an increased resistance to flow. One way to characterize the flow behavior of suspensions is through their apparent or *effective* viscosity (μ_{eff}) [33] with the seminal result $\mu_{eff}=\mu\left(1+2.5\langle\phi\rangle\right)$ due to Einstein [34] for dilute (i.e. non-interacting) and uniformly distributed small spherical particles in a Newtonian liquid with viscosity $\mu=\rho\nu$. This result can be obtained through analyses of energy dissipation rates in sheared systems [34] and also based on stress considerations [35]. We acknowledge that the particles considered in the current study are neither distributed homogeneously, nor small (in the sense of particle-based Reynolds numbers of less (much) than 1), nor dilute, and nor – in many cases – spherical. Still, we use an Einstein-type relation in a heuristic sense by introducing a coefficient α to characterize the viscous behavior of the suspensions: $\mu_{eff}=\mu\left(1+\alpha\langle\phi\rangle\right)$; for simplicity and in order to deal with a single parameter α, we do not consider higher order terms in $\langle\phi\rangle$ as in [36] or other more extensive suspension viscosity models. Our simulation results we use to determine the dependence of α on Re, $\langle\phi\rangle$ and the particle type.

The coefficient α has been extracted from the simulations by monitoring the time-average volumetric flow rate φ_V (of solids and liquid combined), then calculating $\mu_{eff} = \frac{f_x W H^3}{12\varphi_V}$ and finally $\alpha = \left(\frac{\mu_{eff}}{\mu} - 1\right) \Big/ \langle\phi\rangle$. In line with Happel & Brenner [33] we also determined μ_{eff} through comparing the energy dissipation rate of the particulate system (E^*) with that of the fluid-only system (E): $\mu_{eff}/\mu = E^*/E$. The α determined this way was within 3% of the one from the volumetric flow rate.

For spherical particles, results are presented in Figure 8: α as a function of $\langle\phi\rangle$ for all Reynolds numbers considered. The strongest trend in these results is the one with the Reynolds number: a very significant decrease in α with decreasing Reynolds number. Furthermore, one observes – at least for $\mathrm{Re} \le 60$ – a slight minimum in α as a function of $\langle\phi\rangle$. This we believe reflects the transition from preferential concentration at the stable sphere locations, via a fairly uniform $\phi(z)$, to core peaking of the solids volume fraction profile (see Figure 5).

The strong reduction of α with a reduction in Re we try to interpret in terms of stresses. A fluid-only Poiseuille flow has a shear stress profile of $\sigma_{xz} = f_x\left(z - H/2\right)$. Adding particles to the flow creates additional sources of momentum transfer (i.e. stress) in the *z*-direction [26]: fluid and particle streaming as well as momentum transfer as a result of particle-particle and particle-wall interactions (in our simulations these are collisions and lubrication forces). These additional stress mechanisms lead to an increased apparent (effective) viscosity as compared to the liquid-only viscosity. For a typical case ($\langle\phi\rangle = 0.1$, $\mathrm{Re} = 150$) we show in the left panel of Figure 9 the three stress contributions due to the presence of the spheres. The way the stress profiles $\sigma_{xz}(z)$ have been determined has been described in

[26]. It can be seen that the particle-particle and particle-wall (ppw) interactions are by far the main source of additional stress. The middle panel of Figure 9 shows that the ppw-stress is a strong function of the Reynolds number and in that sense might explain the dependence of α on the Reynolds number. The right panel of Figure 9 shows how the ppw-stress depends on the overall solids volume fraction. Crudely speaking it does so in a way linear with $\langle\phi\rangle$ which to some level supports our choice for a linear relationship between $\langle\phi\rangle$ and excess viscosity. We note that ppw-stress calculations depend on short-range interaction modeling. Figure S1 (Supporting material) gives an impression – for one case – of how sensitive the stress is to three of these parameters.

In discussing the effective viscosity of cylinder suspensions we focus on the role of the particle's aspect ratio ℓ/d_c. Figure 10 shows α as a function of $\langle\phi\rangle$ at $\mathrm{Re}=150$. Different from sphere suspensions there is a clear trend: α gets smaller as $\langle\phi\rangle$ increases which hints at an effect of particle orientation since a similar trend was not found with spheres. Cylinders strongly orient at low $\langle\phi\rangle$ and loose their preferential orientation due to particle-particle interaction at higher $\langle\phi\rangle$; see Figures 6 and 7. The disks (ℓ/d_c =0.5) have consistently higher α than the other cylinders considered. However, when we get to $\langle\phi\rangle$=0.1, α is not much difference between the different cylinder types.

5. CONCLUSIONS

This paper reports on numerical simulations of laminar solids-liquid flow between two flat parallel plates driven by a body force / pressure gradient. It starts with a single particle and for this reproduces results from the literature [19,20] regarding it preferential position in between the plates and – for a cylindrical particle – its orientation relative to the direction of shear. By increasing the number of particles, one observes a gradual transition of the solids volume fraction profile from preferential solids concentrations near the stable, single-particle locations to a preference for the middle of the channel. A similar effect has been observed in experimental studies with spherical particles [13,14] where the transition depended in the same way as in the simulations on the overall solids volume fraction $\langle\phi\rangle$ and the Reynolds number.

Cylinders with aspect ratio $\ell/d_c \leq \frac{2}{3}$ preferentially orient with their centerline aligned with the shear (y) direction, thereby rotating (spinning) around that centerline. The orientation distribution gets less pronounced with an increasing solids volume fraction due to direct particle-particle interaction (collisions) as well as liquid flow disturbances due to surrounding particles. Cylinders with $\ell/d_c \geq \frac{3}{2}$ evolve such that their centerline gets perpendicular to the shear direction and then tumble through the channel. As for $\ell/d_c \leq \frac{2}{3}$ cylinders, also $\ell/d_c \geq \frac{3}{2}$ cylinder orientation distributions get wider if the solids volume fraction is increased. In the range $\frac{3}{2} > \ell/d_c > \frac{2}{3}$ the eventual orientation of a single cylinder can be either tumbling or spinning, dependent on its initial condition.

Irrespective of the type of particle, we observe a reduction in the volumetric flow rate upon adding more particles. This increased flow resistance we quantify as an increase of the effective viscosity μ_{eff} of the solids-liquid mixture. Subsequently we have been using the following ansatz – inspired by [33,34] – for scaling the change from single-phase viscosity μ to the effective viscosity: $\mu_{eff} = \mu\left(1+\alpha\langle\phi\rangle\right)$ with $\langle\phi\rangle$ the overall solids volume fraction. For spheres suspensions it was shown that this scaling fairly well captures the effect of $\langle\phi\rangle$; for any of the Reynolds numbers investigated, α varies by not more than 30% over a $\langle\phi\rangle$-range from 0.01 to 0.15 (this maximum variation is at Re=30). We do, however, observe a systematic trend with α going through a minimum at $\langle\phi\rangle$ values just below the transition to core peaking of solids volume fraction profiles $\phi(z)$.

The coefficient α for spheres suspensions strongly depends on the channel's Reynolds number: it gets smaller by almost a factor of 3 from Re=150 to Re=15. It was demonstrated that this can be attributed to the particles strongly contributing to momentum transfer in the wall-normal (z) direction, in particular the forces that are associated to short-range particle-particle and particle-wall interactions (lubrication and collision), which was shown to be a profound function of the Reynolds number.

For cylinder suspensions at Re=150 the trend of α with increasing $\langle\phi\rangle$ is a monotonic decay that tentatively relates to effects of preferential orientation. Orientation distributions are very pronounced for low $\langle\phi\rangle$ and widen significantly if $\langle\phi\rangle$ increases.

This study shows how the quality of particle focusing in (micro) fluidic devices might get impacted by the presence of other particles that lead to defocusing and, eventually, to particles preferring the middle of the channel, irrespective of their size or shape. With this in mind, an avenue of future work is to have multiple particle sizes and/or shapes in a Poiseuille flow device and study how discriminate the device is in these respects.

It should be noted that the above is purely a computational exercise. Although we have confidence in the numerical method from past experience, including experimental validation of the simulation approach used [37,38], and given the agreement with single-particle migration results from the literature [19,20], an experimental program probing the transitions observed (e.g. defocusing and core peaking of concentration profiles; widening of orientation angle distribution of non-spherical particles) would be a meaningful and therefore critical exercise.

References

[1] Marchioli C, Bourgoin M, Coletti F, Fox R, Magnaudet J, Reeks M, Simonin O, Sommerfeld M, Toschi F, Wang L-P, Balachandar S. Particle-laden flows. Int J Multiphase Flow. 2025; 19: 105291–1–31.

[2] Schonberg JA, Hinch EJ. Inertial migration of a sphere in Poiseuille flow. J Fluid Mech. 1989; 203: 517–524.

[3] Chun B, Ladd AJC. Inertial migration of neutrally buoyant particles in a square duct: An investigation of multiple equilibrium positions. Phys Fluids. 2006; 18: 031704-1–4.

[4] Matas JP, Morris JF, Guazzelli É. Inertial migration of rigid spherical particles in Poiseuille flow. J Fluid Mech. 2004; 515; 171–195.

[5] Matas JP, Morris JF, Guazzelli É. Lateral force on a rigid sphere in large-inertia laminar pipe flow. J Fluid Mech. 2009; 621; 59–67.

[6] Leighton D, Acrivos A. The shear-induced migration of particles in concentrated suspensions. J Fluid Mech. 1987; 181: 415–439.

[7] Saffman PG. On the motion of small spheroidal particles in a viscous liquid. J Fluid Mech. 1956; 1: 540–553.

[8] Saffman PG. The lift on a small sphere in a slow shear flow. J Fluid Mech. 1965; 22: 385–400; Saffman, P. G. Correction. J. Fluid Mech. 1968; 31: 624.

[9] Segré G, Silberberg A. Behaviour of macroscopic rigid spheres in Poiseuille flow. Part 2. Experimental results and interpretation. J Fluid Mech 1962; 14: 136–157.

[10] Di Carlo D, Irimia D, Tompkins RG, Toner, M. Continuous inertial focusing, ordering, and separation of particles in microchannels. PNAS. 2007; 104: 18892–18897.

[11] Di Carlo D, Edd JF, Humphry KJ, Stone HA, Toner M. Particle segregation and dynamics in confined flows. Phys Rev Letters. 2009; 102: 0945032009-1–4.

[12] Hur SC, Choi S-E, Kwon S, Di Carlo D. Inertial focusing of non-spherical microparticles. Appl Phys Lett. 2011; 99: 044101-1–3.

[13] Han M, and Kim C. Particle migration in tube flow of suspensions. J Rheol. 1999; 43: 1157–1174.

[14] Snook B, Butler JE, Guazzelli É. Dynamics of shear-induced migration of spherical particles in oscillatory pipe flow. J Fluid Mech. 2016; 786: 128–153.

[15] Masaeli M, Sollier E,,1,2, Amini H, Mao W, Camacho K, , Doshi N, Mitragotri S, Alexeev A, Di Carlo D. Continuous inertial focusing and separation of particles by shape. Phys Rev X. 2012; 2: 031017-1–13.

[16] Feng J, Hu HH, Joseph DD. Direct simulation of initial value problems for the motion of solid bodies in a Newtonian fluid. Part 2. Couette and Poiseuille flows. J Fluid Mech. 1994; 277: 271–301.

[17] Ladd AJC. Numerical simulations of particle suspensions via a discretized Boltzmann equation. Part 1. Theoretical Foundation. J Fluid Mech. 1994; 271: 285–309.

[18] Ladd AJC. Numerical simulations of particle suspensions via a discretized Boltzmann equation. Part 2. Numerical results. J Fluid Mech. 1994; 271: 311–339.

[19] Asmolov ES, Dubov AL, Nizkaya TV, Harting J, Vinogradova OI. Inertial focusing of finite-size particles in microchannels. J Fluid Mech. 2018; 840: 613–630.

[20] Nizkaya TV, Gekova AV, Harting J, Asmolov ES, Vinogradova OI. Inertial migration of oblate spheroids in a plane channel. Phys Fluids. 2020; 32: 112017-1–7.

[21] Succi S. The lattice Boltzmann equation for fluid dynamics and beyond. Oxford: Oxford University Press; 2001.

[22] Somers JA. Direct simulation of fluid flow with cellular automata and the lattice-Boltzmann equation. Applied Scientific Research. 1993;51: 127–133.

[23] Eggels JGM, Somers JA. Numerical simulation of free convective flow using the lattice-Boltzmann scheme. Int J Heat & Fluid Flow. 1995; 16: 357–364.

[24] Peskin CS. Flow patterns around heart valves – Numerical methods. J Comp Phys. 1972; 10: 252–271.

[25] Ten Cate A, Nieuwstad CH, Derksen JJ, Van den Akker HEA. PIV experiments and lattice-Boltzmann simulations on a single sphere settling under gravity. Phys Fluids. 2002; 14: 4012–4025.

[26] Derksen JJ, Sundaresan S. Direct numerical simulations of dense suspensions: wave instabilities in liquid-fluidized beds. J Fluid Mech. 2007; 587: 303–336.

[27] Kim S, Karrila SJ. Microhydrodynamics: Principles and Selected Applications. Butterworth–Heinemann; 1991.

[28] Nguyen N-Q, Ladd, AJC. Lubrication corrections for lattice-Boltzmann simulations of particle suspensions. Phys. Rev. E. 2002; 66: 046708.

[29] Derksen JJ. Liquid fluidization with cylindrical particles: Highly resolved simulations. AIChE Journal 2019; 65: e16594.

[30] Li J, Zhang L, Han K, Lin S, Lu J, Liu, F, Derksen JJ. Cylinders intruding wet granular beds – experiment and simulation J Hydraulic Res. 2024; 62: 351–364.

[31] Shardt O, Derksen JJ. Direct simulations of dense suspensions of non-spherical particles. Int J Multiphase Flow. 2012; 47: 25–36.

[32] Kuipers JB. Quaternions and Rotation Sequences. Princeton: Princeton University Press; 1999.

[33] Happel J, Brenner, H. Low Reynolds number hydrodynamics. The Hague: Martinus Nijhoff Publishers; 1983.

[34] Einstein A. The theory of Brownian movement. New York: Dover; 1956.

[35] Burgers JM. Second report on viscosity and plasticity. Amsterdam: North Holland; 1938.

[36] Simha R. A treatment of the viscosity of concentrated suspensions. J Applied Physics. 1952; 23: 1020–1024.

[36] Li G, Li Z, Gao Z, Wang J, Bao Y, Derksen JJ. Particle image velocimetry experiments and direct numerical simulations of solids suspension in transitional stirred tank flow. Chem Engng Sc. 2018; 291: 288–299.

[37] Derksen JJ. Bending and low-frequency vortex shedding of flexible cylinders in laminar shear flow. AIChE J. 2021; 67: pe17268.

Figures

Figure 1. Timeseries of the z-location of the centers of single spheres in planar Poiseuille flow at a selection of Reynolds numbers and starting locations z_0 as indicated. The insets reflect instants at the end of two of the time series, including color contours of velocity magnitude.

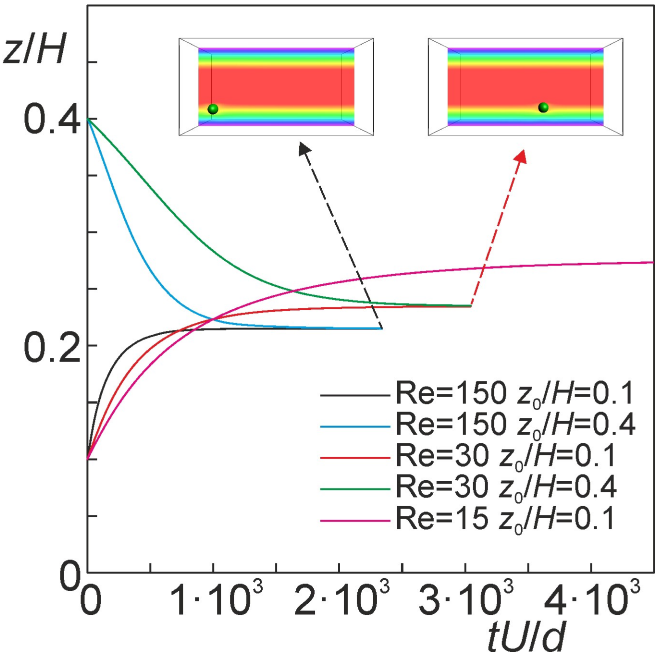

Figure 2. Top: three time series of the z-location of the centers of single cylinders with $\ell/d_c=1$ and equivalent diameter d_e; cylinders with different initial orientation vectors $\mathbf{a}_0$, all cylinders start $z_0/H=0.1$. The insets show eventual situations (tumbling left, spinning right). Bottom: time series of orientation vector components a_x (blue) and a_y (black) for the case $\mathbf{a}_0=\left(-\frac{1}{3},\frac{2}{3},\frac{2}{3}\right)$ showing the cylinder evolving to a tumbling motion. $\mathrm{Re}=150$.

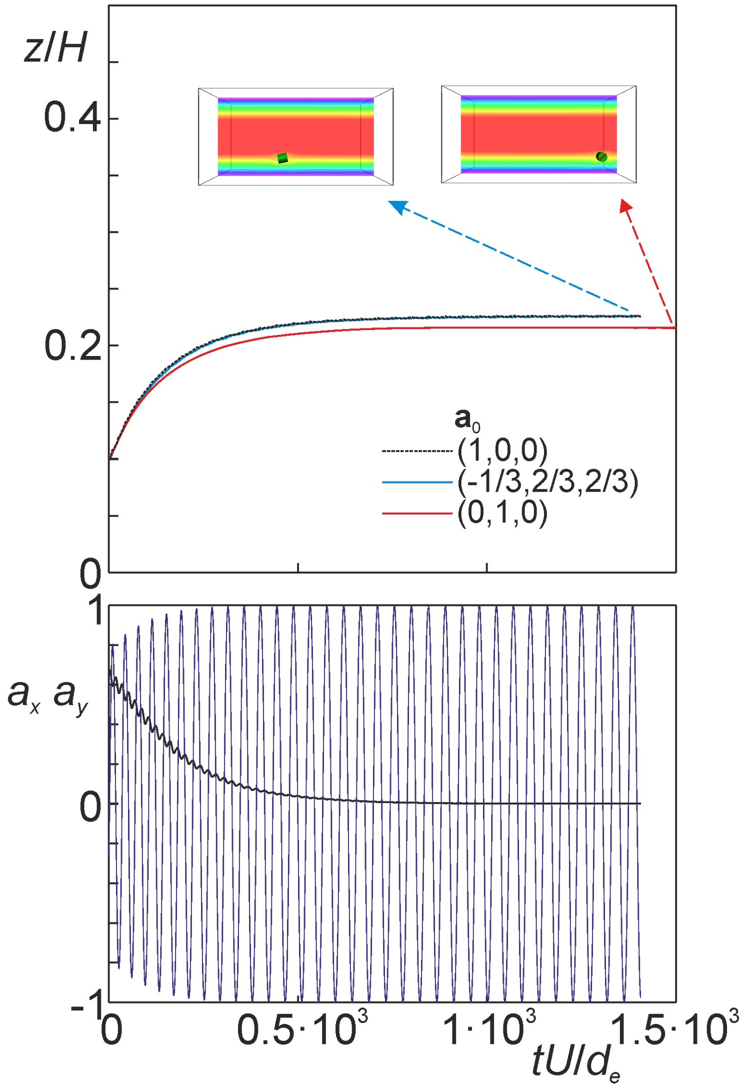

Figure 3. Top: time series of a single cylinder with $\ell/d_c = \frac{1}{2}$ starting with $\mathbf{a}_0 = (1,0,0)$ at $\mathrm{Re} = 150$ (black) and $\mathrm{Re} = 30$ (red). Bottom: a cylinder with $\ell/d_c = \frac{3}{2}$ (black) and one with $\ell/d_c = 2$ (red) both starting with $\mathbf{a}_0 = (0,1,0)$ and at $\mathrm{Re} = 150$.

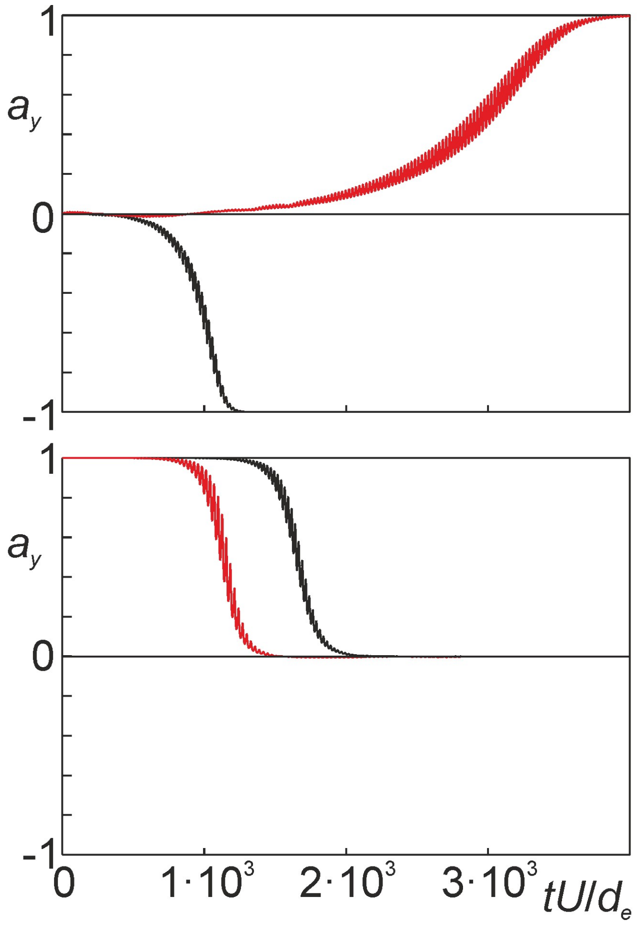

Figure 4. Left: impressions of multi-sphere systems at $\mathrm{Re}=150$ and with $\langle\phi\rangle=0.0125$, 0.025, 0.10, & 0.15 (top to bottom). Right: corresponding vertical solids volume fraction profiles averaged (after steady state was reached) over time and over the homogeneous (x and y) directions; the profile with $\langle\phi\rangle=0.025$ compares starting times of averaging $tU/H=1.1\cdot10^3$ (black) and $3.3\cdot10^3$ (red). The lower-left panel defines the coordinate system. The Reynolds numbers based on the superficial velocity are (top to bottom) $\mathrm{Re}_{sup}=u_{sup}H/\nu=97$, 93, 78, 70.

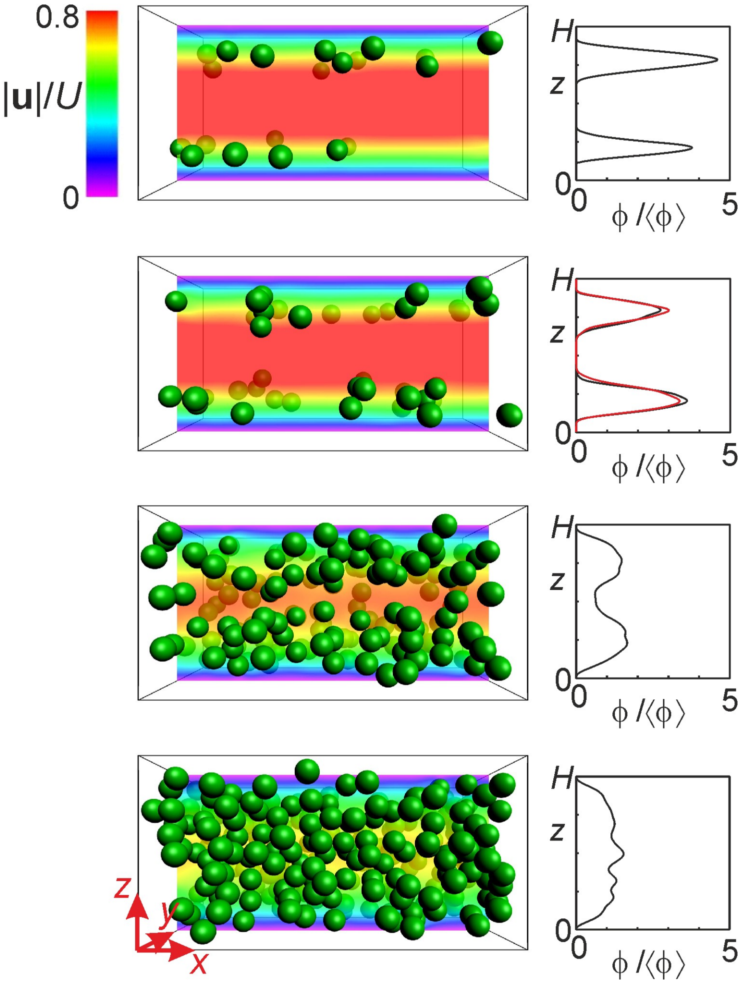

Figure 5. Average solids concentration profiles for spheres over the channel height; effect of Reynolds number and overall solids volume fraction as indicated per panel. The dashed vertical lines in the top row profiles indicate single sphere equilibrium positions. The color insets have the same color scale as the color images in Figure 4.

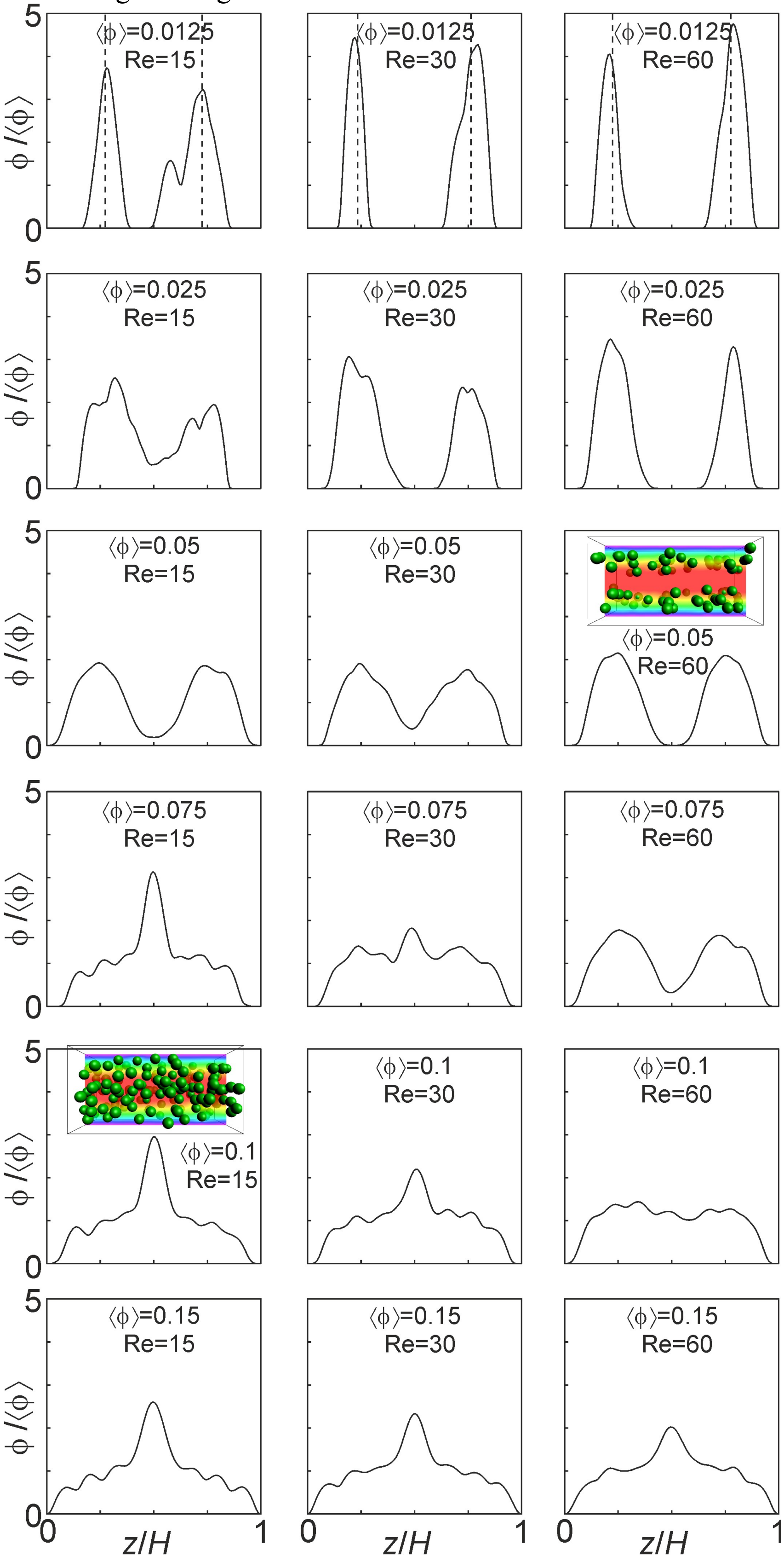

Figure 6. Multi-cylinder systems at (left) $\mathrm{Re}=150$ and (right) $\mathrm{Re}=30$. All cases shown have $\ell/d_c=1$. From bottom to top the overall solids volume fraction increases: $\langle\phi\rangle=0.025$, 0.05 and 0.15 respectively. Of each case we show a snapshot with the colors denoting liquid velocity magnitude, the vertical solids volume fraction profile $\phi(z)$, and the orientation distribution of the cylinders with ψ_y the angle between the cylinder axis and the shear (i.e. y) direction. The blue symbols are simulations data; the red curve is $\sin\psi_y$ which is what an isotropic orientation distribution would look like.

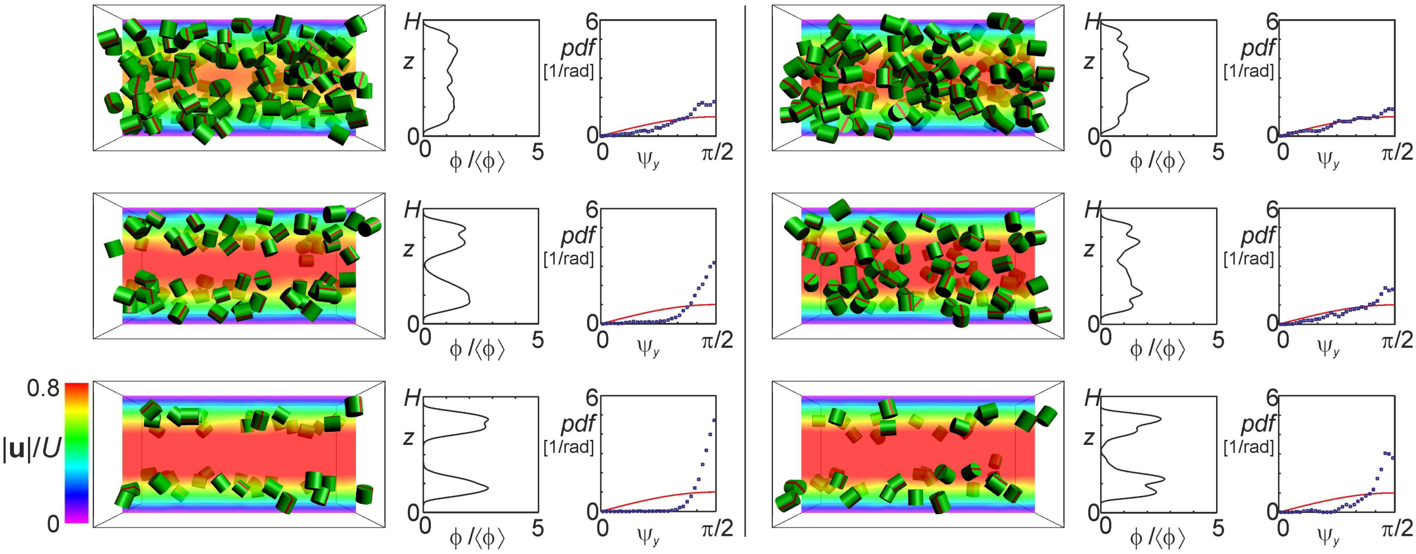

Figure 7. Multi-cylinder systems at $\mathrm{Re}=150$. Left: $\ell/d_c=0.5$; right $\ell/d_c=2$. From bottom to top $\langle\phi\rangle=0.025$, 0.05 and 0.15 respectively. For each case we show a snapshot, the solids volume fraction profile $\phi(z)$ and the orientation angle (ψ_y) distribution.

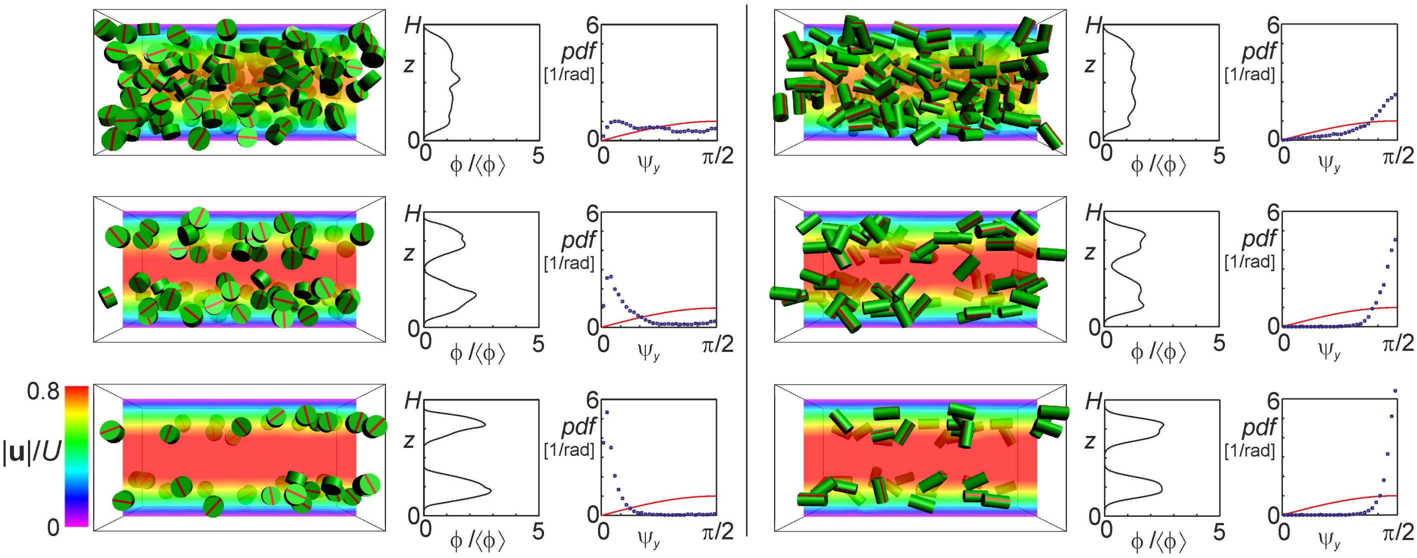

Figure 8. Viscosity coefficient α (as defined in the text) for spheres-systems as a function of overall solids volume fraction $\langle \phi \rangle$ for various Reynolds numbers as indicated.

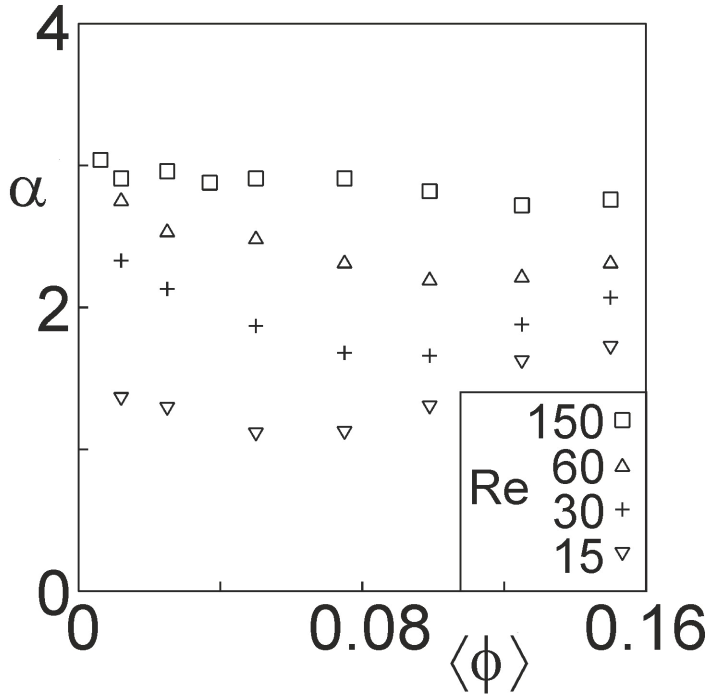

Figure 9. Shear stress σ_{xz} (non-dimensionalized by the body force and channel half height $f_x H/2$) distribution over the channel height for spheres systems. Left: stress contributions (ppw is particle-particle & particle-wall interaction, ps is particle streaming, fs is fluid streaming) for $\mathrm{Re}=150$ and $\langle\phi\rangle$=0.1; middle: pp-stress at $\langle\phi\rangle$=0.1 for various Re; right: pp-stress at $\mathrm{Re}=150$ for various $\langle\phi\rangle$.

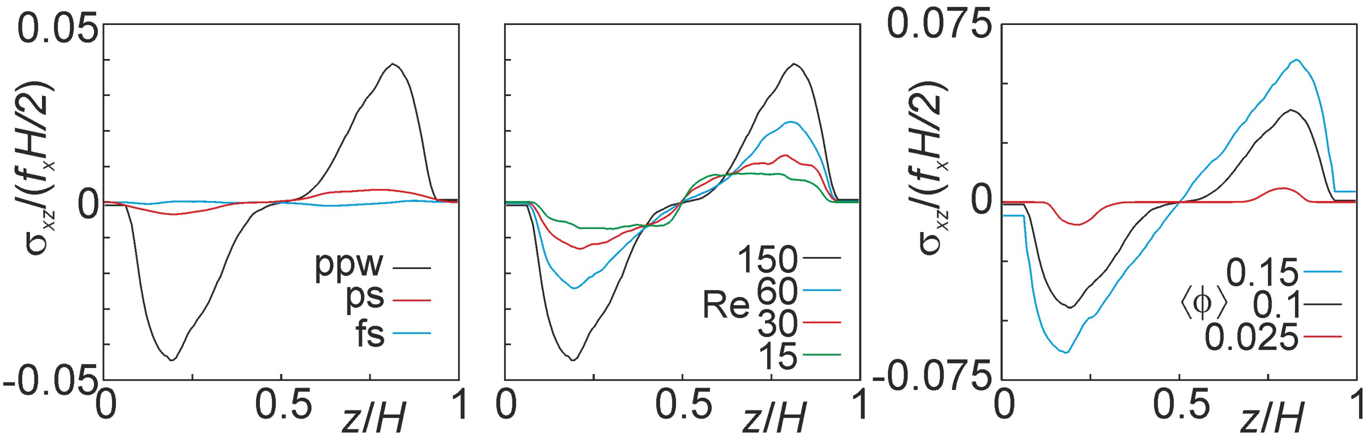

Figure 10. Viscosity coefficient α (as defined in the text) for cylinder-systems at $\mathrm{Re}=150$ as a function of overall solids volume fraction $\langle\phi\rangle$ for various ℓ/d_c ratios as indicated.